Icarus 415 (2024) 116079

Contents lists available at ScienceDirect

Icarus

journal homepage: www.elsevier.com/locate/icarus

The lunar $^{40}Ar/^{36}Ar$ antiquity indicator in the presence of a lunar paleomagnetosphere

A.R. Poppe [a,*], I. Garrick-Bethell [b], S. Fatemi [c], C. Grava [d]

[a] Space Sciences Laboratory, University of California at Berkeley, Berkeley, CA 94720, USA
[b] Department of Earth and Planetary Sciences, University of California Santa Cruz, Santa Cruz, CA, USA
[c] Department of Physics, Umeå University, Umeå, Sweden
[d] Southwest Research Institute, San Antonio, TX, USA

ARTICLE INFO

Keywords:
The moon (1692)
Lunar magnetic fields (960)
Planetary magnetospheres (997)
Solar wind (1534)

ABSTRACT

The ratio of $^{40}Ar/^{36}Ar$ trapped within lunar grains, commonly known as the lunar antiquity indicator, is an important semi-empirical method for dating the time at which lunar samples were exposed to the solar wind. The behavior of the antiquity indicator is governed by the relative implantation fluxes of solar wind-derived ^{36}Ar ions and indigenously sourced lunar exospheric ^{40}Ar ions. Previous explanations for the behavior of the antiquity indicator have assumed constancy in both the solar wind ion precipitation and exospheric ion recycling fluxes; however, the presence of a lunar paleomagnetosphere likely invalidates these assumptions. Furthermore, most astrophysical models of stellar evolution suggest that the solar wind flux should have been significantly higher in the past, which would also affect the behavior of the antiquity indicator. Here, we use numerical simulations to explore the behavior of solar wind ^{36}Ar ions and lunar exospheric ^{40}Ar ions in the presence of lunar paleomagnetic fields of varying strengths. We find that paleomagnetic fields suppress the solar wind ^{36}Ar flux by up to an order-of-magnitude while slightly enhancing the recycling flux of lunar exospheric ^{40}Ar ions. We also find that at an epoch of ~2 Gya, the suppression of solar wind ^{36}Ar access to the lunar surface by a lunar paleomagnetosphere is–somewhat fortuitously–nearly equally balanced by the expected increase in the upstream solar wind flux. These counterbalancing effects suggest that the lunar paleomagnetosphere played a critical role in preserving the correlation between the antiquity indicator and the radioactive decay profile of indigenous lunar ^{40}K. Thus, a key implication of these findings is that the accuracy of the $^{40}Ar/^{36}Ar$ indicator for any lunar sample may be strongly influenced by the poorly constrained history of the lunar magnetic field.

1. Introduction

Laboratory analyses of returned lunar samples have shown varying levels of trapped noble gases within grain interiors including the ^{36}Ar and ^{40}Ar isotopes (e.g., Wieler, 1998; Wieler and Heber, 2003; Wieler, 2016). It was recognized early that while implanted ^{36}Ar originates from the solar wind, the presence of ^{40}Ar likely originates from the radioactive decay and outgassing of primordial lunar ^{40}K within the Moon's interior (e.g., Heymann et al., 1970). Once outgassed into the lunar exosphere, neutral ^{40}Ar atoms are ionized and picked up by the solar wind or terrestrial magnetospheric fields, with a typical fraction of ~50% of the ions re-implanted into the lunar regolith (e.g., Manka and Michel, 1970; Poppe et al., 2013). It was further observed that the ratio of implanted ^{40}Ar to ^{36}Ar within a grain correlated strongly with the grain exposure age (e.g., Yaniv and Heymann, 1972; Podosek and Huneke, 1973; Reynolds et al., 1974; McKay et al., 1986), where the exposure age–or 'antiquity'–is the discrete time at which the grain was exposed to the solar wind, *not* the integrated time of exposure. To first order, the $^{40}Ar/^{36}Ar$ ratio correlates with the radioactive decay rate of primordial ^{40}K with a half-life of 1.28 Ga, further suggesting the origin of the parentless ^{40}Ar to be from internal ^{40}K. For example, 'young' lunar material possesses a $^{40}Ar/^{36}Ar$ ratio of ~0.5, while some of the oldest-known samples from ~3.7 Gya possess $^{40}Ar/^{36}Ar$ ratios of ~14 (e.g., Reynolds et al., 1974). Later work established more rigorous empirical calibrations of the $^{40}Ar/^{36}Ar$ ratio, often termed the lunar 'antiquity indicator', based on separate radio-chronological dating methods (e.g., $^{235}U–^{136}Xe$) (e.g., Eugster et al., 2001; Joy et al., 2011). Such a dating method provides an important tool in understanding the timing, evolution, and relative ordering of processes such as the flux of planetary impactors to the inner solar system (e.g., Joy et al., 2012), the flux of solar and cosmic radiation in the inner heliosphere (e.g., Becker

* Corresponding author.
E-mail address: poppe@berkeley.edu (A.R. Poppe).

https://doi.org/10.1016/j.icarus.2024.116079
Received 15 September 2023; Received in revised form 9 February 2024; Accepted 3 April 2024
Available online 6 April 2024

and Pepin, 1989; Wieler et al., 1999), and the rates of meteoritic and regolith space weathering at the Moon (e.g., Eugster et al., 1991; Lucey et al., 2006).

While the close correlation of the $^{40}Ar/^{36}Ar$ ratio with the ^{40}K decay half-life would suggest a simple and easily understood mechanism underpinning the antiquity indicator, such a conclusion is built upon (at least) three separate assumptions (e.g., Heymann et al., 1970; Yaniv and Heymann, 1972; Eugster et al., 2001):

1. The effusion rate of ^{40}Ar neutrals from the lunar interior follows a direct (or near direct) relationship with the radioactive decay rate of ^{40}K from the lunar interior. In other words, the outgassing efficiency of ^{40}Ar has not changed over geologic time.
2. The flux of solar wind $^{36}Ar^{+}$ ions to the lunar surface has stayed constant (or near constant) over geologic time.
3. The recycling efficiency of ionized $^{40}Ar^{+}$ ions back into the lunar soil has remained constant (or near constant) over geologic time.

If all three assumptions hold, then the apparent correlation of the $^{40}Ar/^{36}Ar$ ratio with the ^{40}K decay half-life holds as well. Nevertheless, as discussed below and as the prime focus of this study, these assumptions may indeed *not* hold, thereby forcing us to reassess the fundamental processes at work in generating the observed behavior of the $^{40}Ar/^{36}Ar$ ratio within lunar samples. In particular, assumptions #2 and #3 regarding the flux of solar wind $^{36}Ar^{+}$ and lunar exospheric $^{40}Ar^{+}$ ions to the lunar surface should be reevaluated due to the role that lunar paleomagnetic fields likely played in shaping the behavior and dynamics of these ions. We do acknowledge that despite revisiting these two assumptions the first-order agreement between the $^{40}Ar/^{36}Ar$ ratio and measures of various samples' exposure ages (e.g., Eugster et al., 2001) nonetheless suggests that–even empirically–the lunar antiquity indicator remains a useful tool for lunar sample analysis. Finally, we also note that assumption #1 regarding the outgassing of radiogenic ^{40}Ar from the lunar interior deserves reconsideration as well, given uncertainties in the source regions and mechanisms by which ^{40}Ar may outgas (e.g., Killen, 2002; Grava et al., 2015; Wieler, 2016); however, such a reanalysis is beyond the scope of this study.

It is also worth noting that an interpretation of the $^{40}Ar/^{36}Ar$ ratio within a given sample as a measure of such sample's exposure age also relies on several other assumptions. First, an accurate interpretation of the $^{40}Ar/^{36}Ar$ ratio of a sample generally requires a 'simple' exposure history, where a given sample was only exposed to the solar wind once over its lifetime. Samples with 'complex' exposure histories, i.e., where multiple distinct exposures occur at separate epochs, will blend together different values of the $^{40}Ar/^{36}Ar$ ratio and thus, muddle any interpretation. Lunar samples with complex histories have been noted in cosmic ray exposure ages of lunar samples (e.g., Eugster, 2003; Merle et al., 2017; Curran et al., 2019). Second, one must assume that the length of exposure of a given lunar sample to the solar wind must be long with respect to any natural variations in both the ^{40}Ar and ^{36}Ar fluxes. In the case of ^{40}Ar, the recycling time of an individual atom within the exosphere (i.e., the time elapsed from when it first outgassed to when it was ionized and reimplanted) is on the order of 20 days under current solar irradiation conditions (higher solar irradiance at younger ages would only shorten this timescale). Additionally, seasonal (i.e., yearly) variations in the ^{40}Ar content of the exosphere have been previously noted (e.g., Benna et al., 2015; Kegerreis et al., 2017), perhaps due to variability in the size of regional cold traps, which can temporarily harbor or release argon atoms. Nevertheless, both daily and yearly scale variations in the ^{40}Ar content and flux at the Moon would be long since averaged over on the typical scales expected for lunar sample exposure on the lunar surface. The same argument applies for solar wind-derived ^{36}Ar which should follow solar cycle variations on the 11-year Hale cycle, again much shorter than expected exposure intervals. Third, one must also assume that the exposure time of a sample is less than the long-term secular variation in both the ^{36}Ar and ^{40}Ar fluxes at the Moon. The timescale for secular ^{40}Ar variation is set by the 1.25 Byr half-life of ^{40}K, while the secular variation in the solar wind-derived ^{36}Ar is less well constrained (and is discussed further in Section 3), yet likely in the range of several 10^8 years. Thus, so long as a sample is assumed to be exposed to the solar wind for timescales $<\sim 10^8$ years, it will record a single value for the $^{40}Ar/^{36}Ar$ ratio corresponding to time at which lunar samples were exposed to the solar wind (its "exposure age"). Finally, other physical effects such as micrometeoroid bombardment of the lunar surface can locally affect the $^{40}Ar/^{36}Ar$ ratio within a given sample; however, as is apparent from previous empirical studies that show a first-order correlation between the $^{40}Ar/^{36}Ar$ ratio and a sample's antiquity (e.g., Eugster et al., 2001), such destruction processes cannot be fully erasing the argon content of many samples.

As inferred from the presence of remanent magnetization observed in lunar meteorites and returned samples as well as from orbital in-situ measurements, the Moon likely possessed a dynamo and thus, a paleomagnetic field, through a large part of its lifetime (e.g., Garrick-Bethell et al., 2009; Weiss and Tikoo; Tikoo et al., 2017). Within the first billion years of the Moon's lifetime, measurements indicate extraordinarily large field strengths up to $\sim$100 μT (e.g., Cournède et al., 2012; Shea et al., 2012; Garrick-Bethell et al., 2017; Garrick-Bethell and Kelley, 2019; Wakita et al., 2021); however, such strong fields may have been episodic rather than continuous (Evans and Tikoo, 2022). After this early high-field epoch, the Moon may have possessed a long-lived yet relatively weaker dynamo and paleomagnetic field strength of $\sim$5 μT (Tikoo et al., 2017). Finally, by at least 1 Gya, sample analysis demonstrates that the lunar dynamo ceased to operate (Mighani et al., 2020). Today, the Moon possesses only local or regional remanent crustal magnetic fields widely dispersed across its surface, although some such fields can reach strengths of hundreds of nanotesla, at minimum (e.g., Dyal et al., 1974; Hood et al., 2001; Mitchell et al., 2008).

In this manuscript, we challenge assumptions #2 and #3 above regarding the variability of the $^{36}Ar^{+}$ and $^{40}Ar^{+}$ fluxes to the lunar surface over geologic time. We emphasize that we do not dispute the observed correlation between the $^{40}Ar/^{36}Ar$ ratio with the ^{40}K decay half-life as shown in e.g., Eugster et al. (2001), but rather seek to explore the underlying explanation for why such an apparent correlation exists at all. In Section 2, we describe the design of the hybrid plasma simulations conducted to investigate the behavior of both $^{36}Ar^{+}$ and $^{40}Ar^{+}$ as they interact with the lunar paleomagnetosphere. In Section 3, we discuss the flux of solar wind $^{36}Ar^{+}$ to the lunar surface. In particular, we address the potential variability that may have existed in the $^{36}Ar^{+}$ flux to the Moon as a function of (i) the evolution of the Sun and the solar wind (e.g., Wood et al., 2005; Vidotto, 2021) and (ii) the strength of a lunar paleomagnetosphere (e.g., Tikoo et al., 2017; Poppe et al., 2021). In Section 4, we discuss the flux of endogenous lunar $^{40}Ar^{+}$ to the lunar surface via exospheric ionization and recycling, especially as a function of lunar paleomagnetospheric strength. Finally, we analyze and discuss our results in Section 5 and conclude in Section 6.

2. Model description

To model the solar wind and lunar exospheric ion dynamics in the presence of a lunar paleomagnetosphere, we have used the Amitis hybrid plasma model (Fatemi et al., 2017), which has been extensively used in previous investigations of moon-magnetosphere and planetary-solar wind interactions throughout the solar system (e.g., Fatemi and Poppe, 2018; Haviland et al., 2019; Fatemi et al., 2020, 2022; Rasca et al., 2021; Garrick-Bethell et al., 2019; Poppe et al., 2021; Poppe and Fatemi, 2023; Wang et al., 2023). The Amitis model employs the standard hybrid plasma modeling technique of treating ions as discrete macroparticles and electrons as a charge-neutralizing fluid while solving for electromagnetic fields on a three-dimensional Cartesian

grid (e.g., Ledvina et al., 2008). For protons, each modeled macroparticle represents $\sim 10^{22}$ physical protons (we emphasize that this does not mean a modeled proton has the mass or charge of 10^{22} protons, only that it represents the behavior of 10^{22} physical protons). The simulation coordinate system is the standard Solar-Selenocentric-Ecliptic (SSE) frame, where $+\hat{x}$ points from the Moon to the Sun, $+\hat{z}$ points to ecliptic north, and $+\hat{y}$ completes the right-handed set. For all simulations, we included a resistive Moon of radius 1750 km (approximating the true lunar radius of 1738 km) with an interior conductivity of $\sigma = 10^{-7}$ S/m. This interior conductivity is low enough to prevent any induced fields and/or currents within the lunar interior (e.g., Haviland et al., 2019), which are not the subject of this study. Note also that the model does not apply any scale renormalization for the applied simulation parameters, i.e., all values are in standard SI units.

Similar to our earlier investigation of solar wind interactions with the lunar paleomagnetosphere (Poppe et al., 2021), we used upstream solar wind conditions appropriate for a lunar age of ~2 Ga (e.g., Airapetian and Usmanov, 2016). The solar wind was modeled with a density of 30 cm^{-3}, velocity of 550 km/s, and temperature of 2.4×10^5 K (≈20 eV). The interplanetary magnetic field was set to a constant value of $\mathbf{B}$ = [0, +30, 0] nT. Incidentally, these upstream values are quite similar to current-day conditions at Mercury, which Amitis has successfully modeled in previous work (e.g., Fatemi et al., 2020). The paleomagnetic fields were simulated by placing a magnetic dipole at the center of the Moon, oriented along the north ecliptic direction (i.e., $\mathbf{M} = M\hat{z}$) and coincident with the lunar spin vector. We simulated eight paleomagnetic field strengths, including a 0 nT case as a control and seven cases increasing in surface field strength by factors of 2 from 62.5 nT to 4000 nT. The highest paleomagnetic field strength simulated is close to that reported in the literature, i.e., $\sim 5 \pm 2\ \mu$T, for lunar ages of ~1–2.5 Ga (Tikoo et al., 2017). We also performed two additional simulations with the 4000 nT paleomagnetic field strength at two other discrete ages, 1 Gyr and 3 Gyr, in order to quantify the variability in the changes in the lunar antiquity indicator as a function of variable solar wind conditions. Using both the Wood et al. (2005) and Airapetian and Usmanov (2016) studies, we estimated the appropriate solar wind conditions at these two ages. For the 1 Gyr age, we simulated a solar wind density of 140 cm^{-3}, solar wind speed of 650 km/s, interplanetary magnetic field strength of 45 nT, and ion temperature of 25 eV. For the 3 Gyr age, we simulated a solar wind density of 15 cm^{-3}, solar wind speed of 475 km/s, interplanetary magnetic field strength of 17.5 nT, and ion temperature of 15 eV.

In addition to the solar wind protons, we also included the presence of either solar-wind $^{36}Ar^{n+}$ (Section 3) or lunar exospheric $^{40}Ar^{+}$ ions originating from the radioactive decay and outgassing of native lunar ^{40}K (Section 4). Both $^{36}Ar^{+}$ and $^{40}Ar^{+}$ are modeled as macroparticles, similar to solar wind protons, but with macroparticle factors of $\sim 10^{15}$. Furthermore, both argon species are included at their true mass ratio to protons. As described in Poppe et al. (2021), the behavior of solar wind $^{36}Ar^{n+}$ ions was quantified by including synthetic solar wind ions with a charge-to-mass ratio of 0.25 as appropriate for $^{36}Ar^{n+}$ ions with an n =+9 charge state, although we note that the charge states of heavy minor solar wind ions can vary within a couple charges (e.g., von Steiger et al., 2000). The modeled upstream density of solar wind $^{36}Ar^{+}$ ions was set to be small enough such that they represented only a minor species and did not influence the electromagnetic environment. Density distributions and surface precipitation maps for the solar wind $^{36}Ar^{+}$ ions are retrieved from the model after conditions have come to steady-state. Furthermore, we average the surface precipitation maps over an extended interval to ensure that any small-scale temporal variations in the model are sufficiently captured.

To explore the behavior of lunar $^{40}Ar^{+}$ ions within the lunar paleomagnetosphere, we performed a second set of simulations with a source term of $^{40}Ar^{+}$ originating from a neutral ^{40}Ar exosphere. Modern-day measurements have quantified the amount, spatial distribution, and variability of exospheric ^{40}Ar at the Moon (e.g., Hodges and Mahaffy, 2016; Benna et al., 2015; Grava et al., 2015; Kegerreis et al., 2017). After outgassing from the lunar crust, ^{40}Ar neutrals enter a bound lunar exosphere where they remain until lost to surface adsorption within polar cold-trap regions, to interplanetary space via ionization and pickup, or are embedded within lunar soil grains. ^{40}Ar neutrals are generally thermally accommodated to the local lunar surface temperature and nightside lunar temperatures are low enough such that ^{40}Ar neutrals condense out of the exosphere onto the nightside surface (e.g., Hodges et al., 1973, 1974). As the nightside surface of the Moon rotates past the dawn terminator and into sunlight, argon neutrals rapidly desorb from the surface, thereby generating an argon bulge near dawn. Within the hybrid model, we included a continuous $^{40}Ar^{+}$ ionization source derived from the neutral ^{40}Ar modeling results of Grava et al. (2015), with the assumption that the present-day distribution of neutral exospheric argon is representative of that in earlier lunar epochs. Importantly, we primarily take the spatial distribution of ^{40}Ar from the model of Grava et al. (2015); however, we also note that while the Monte Carlo-based modeling results of Grava et al. (2015) are an improvement over earlier assumptions of a spatially uniform Ar exosphere by Manka and Michel (1970), the underlying nature of the Moon's argon exosphere remains similar between the two approaches. Similar to our modeling approach for solar wind $^{36}Ar^{+}$, we set the density of $^{40}Ar^{+}$ low enough such that the ions behave as a minor species and do not disturb the ambient electromagnetic fields. Finally, we note that while both the modeled $^{36}Ar^{+}$ and $^{40}Ar^{+}$ ion densities are modeled as minor species in the hybrid simulations, their fluxes to the lunar surface are appropriately normalized to the 0 nT case in order to properly characterize the effects of a paleomagnetic field on the $^{36}Ar^{+}$ and $^{40}Ar^{+}$ fluxes and their ratio.

3. Assessing the flux of ^{36} Ar^{+} ions to the lunar surface

We first explore possible mechanisms by which the solar wind flux of $^{36}Ar^{+}$ to the lunar surface could have varied over the age of the solar system. In particular, we discuss the evidence for long-term changes in the overall solar wind flux and the impacts such changes would have on the lunar antiquity indicator in Section 3.1. Following this, we discuss the role that a lunar paleomagnetosphere may have had on the precipitation flux of solar wind $^{36}Ar^{+}$ to the lunar surface in Section 3.2.

3.1. Variations in the solar wind ^{36}Ar flux

Among many objects in the solar system, the Moon today is directly exposed to the solar wind, at least for a large fraction of its orbit when outside the terrestrial magnetosphere. Traveling with typical speeds between 250 and 850 km/s (Dmitriev et al., 2011), the solar wind is comprised of primarily protons (~97%) with an assortment of several 'minor' heavy ion species comprising the remaining ~3% (e.g., Bochsler, 1987, 2007). Of this ~3%, ^{4}He dominates followed by O, C, Fe, Si, Ne, N, ^{3}He, and ^{36}Ar in decreasing abundance (i.e., ^{36}Ar is the ninth most abundant minor ion species), with ^{36}Ar possessing an abundance relative to protons of $\sim 2 \times 10^{-6}$. These abundances have been well characterized by various in-situ observations over the length of the modern space age (e.g., Bochsler, 1987, 2000, 2007; Reisenfeld et al., 2007, 2013). Nevertheless, an assessment of the behavior of the lunar antiquity indicator requires accurate knowledge and/or modeling capability of the flux and relative abundance of solar wind $^{36}Ar^{+}$ over the age of the solar system.

Stellar evolution theory dictates that main-sequence stars continually spin down due to angular momentum loss via escaping stellar winds. As a star loses angular momentum, its spin rate and coronal activity decrease, and in turn, the stellar wind flux also decreases (e.g., Wood et al., 2002; Wood, 2004). The coupled stellar spin rate and stellar wind flux continue their decay until a star nears exhaustion of internal hydrogen and exits the main sequence. Within the main-sequence lifetime of stars, multiple lines of evidence support the theory

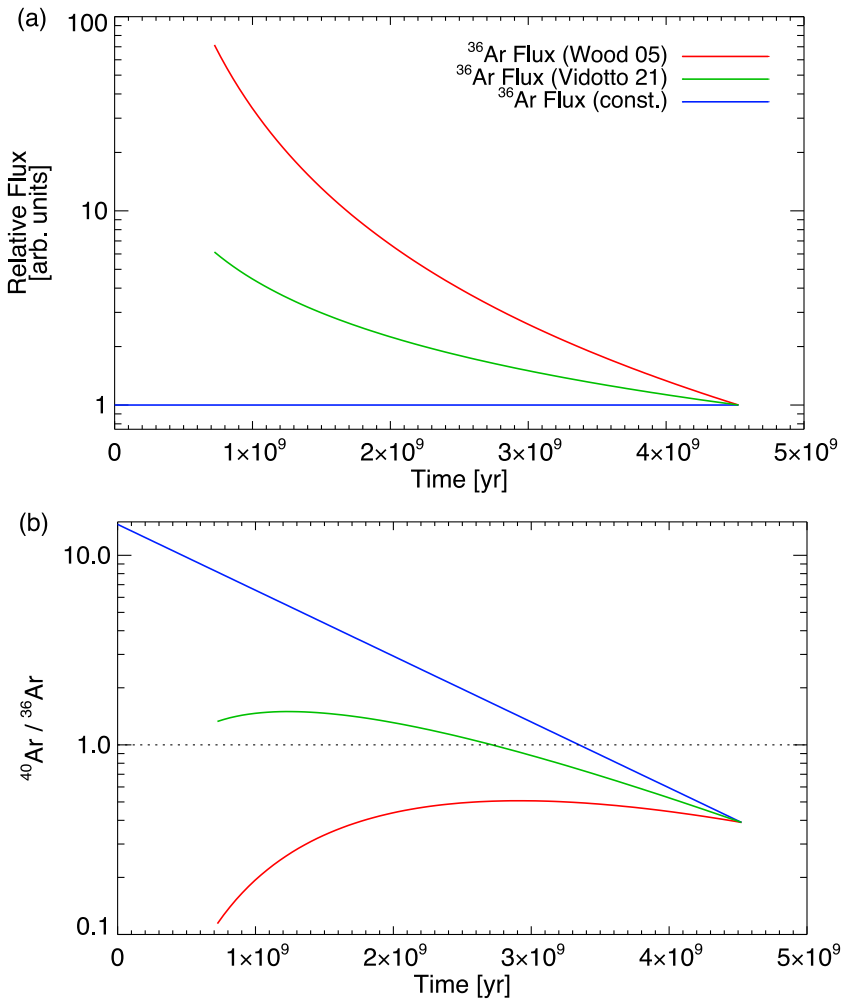

Fig. 1. (a) The variation of solar wind $^{36}Ar^+$ fluxes as a function of solar system age for three assumptions: (blue) constant over time as typically assumed, (green) $\dot{M}_{sw} \propto t^{-0.99}$ (Vidotto, 2021), and (red) $\dot{M}_{sw} \propto t^{-2.33}$ (Wood et al., 2005). For purposes of comparison, all curves are normalized to a value of unity at $t = 4.5$ Gyr. (b) The $^{40}Ar/^{36}Ar$ ratio as a function of time for the same three proposed ^{36}Ar scalings shown in panel (a). The ratios are normalized to a value of 0.39 at $t = 4.5$ Gyr, taken from the $^{40}Ar/^{36}Ar$ ratio measurements in lunar sample 67601 (Kirsten et al., 1973; Eugster et al., 2001).

of decreasing solar wind flux over time (e.g., Geiss and Bochsler, 1991; Wood et al., 2002, 2005; Wood, 2004; Jardine and Collier Cameron, 2019; Vidotto, 2021), although a detailed understanding of the exact behavior of the solar wind flux variation is not yet in hand Obase and Nakashima (e.g., 2023). One method by which to constrain the time evolution of the solar wind flux is to observe or infer the stellar wind properties of solar-like stars of varying ages. For example, Wood et al. (2005) have constrained a collection of stellar wind mass fluxes via remote-sensing detections of Ly-α absorption originating from neutralized stellar wind protons that have undergone charge exchange with local interstellar hydrogen (see also Wood, 2004). Plotted against stellar age (using the observed stellar X-ray flux as an intermediary; e.g., Ayres, 1997; Güdel, 2007), Wood et al. (2005) found a best-fit scaling between stellar wind mass flux and age as, $\dot{M}_{sw} \propto t^{-2.33\pm0.55}$. A later re-analysis of these data combined with an alternative relationship between stellar age and X-ray flux yielded, $\dot{M}_{sw} \propto t^{-0.99}$ (Vidotto, 2021). While the differences between these fits are non-trivial and speak to the current uncertainty in the field of stellar wind evolutionary modeling, they nonetheless both predict stellar wind behavior that decreases in mass flux as a function of time.

How then would a changing solar wind mass flux affect the operation of the lunar antiquity indicator? First, we must assume that any changes in the overall solar wind mass flux affect both solar wind protons and solar wind minor ions equally, noting that the observations of Wood et al. (2005) are strictly speaking only valid for protons. In their discussion of long-term solar variations, Geiss and Bochsler (1991) have argued that an increased solar wind flux in the Sun's past would have resulted in even *less* fractionation between the bulk solar and solar wind compositions, as higher densities in the solar wind source region would imply less effectiveness of any fractionating separation processes. Thus, an assumption that the solar wind minor ion flux closely tracks the overall solar wind proton flux appears justified.

Thus, assuming the fractional composition of solar wind minor ions, including $^{36}Ar^+$, remains the same over the age of the solar system as argued above, we can assess the effects of such an increased flux. Fig. 1(a) compares the relative time variation of solar wind $^{36}Ar^+$ under three separate assumptions: (i) a constant solar wind mass flux over time (blue), (ii) solar wind mass flux scaling as $\dot{M}_{sw} \propto t^{-0.99}$ (Vidotto, 2021, green), and (iii) solar wind mass flux scaling as $\dot{M}_{sw} \propto t^{-2.33}$ (Wood et al., 2005, red). All three curves are normalized to a value of unity at $t = 4.5$ Gyr and are provided only to compare the relative behavior of these three assumptions. Meanwhile, Fig. 1(b) presents the $^{40}Ar/^{36}Ar$ ratio as a function of time for the same three assumptions on the $^{36}Ar^+$ flux, with a normalization such that $^{40}Ar/^{36}Ar = 0.39$ at $t = 4.5$ Gyr as measured in the very recently exposed 67601 sample (Kirsten et al., 1973; Eugster et al., 2001). Note that the Wood et al. (2005) and Vidotto (2021) scalings do not extend earlier than $t = 0.7$ Ga, due to the possibility of a change in the solar wind behavior at this point (e.g., Fionnagáin and Vidotto, 2018). Under the assumption of a constant solar wind $^{36}Ar^+$ flux over

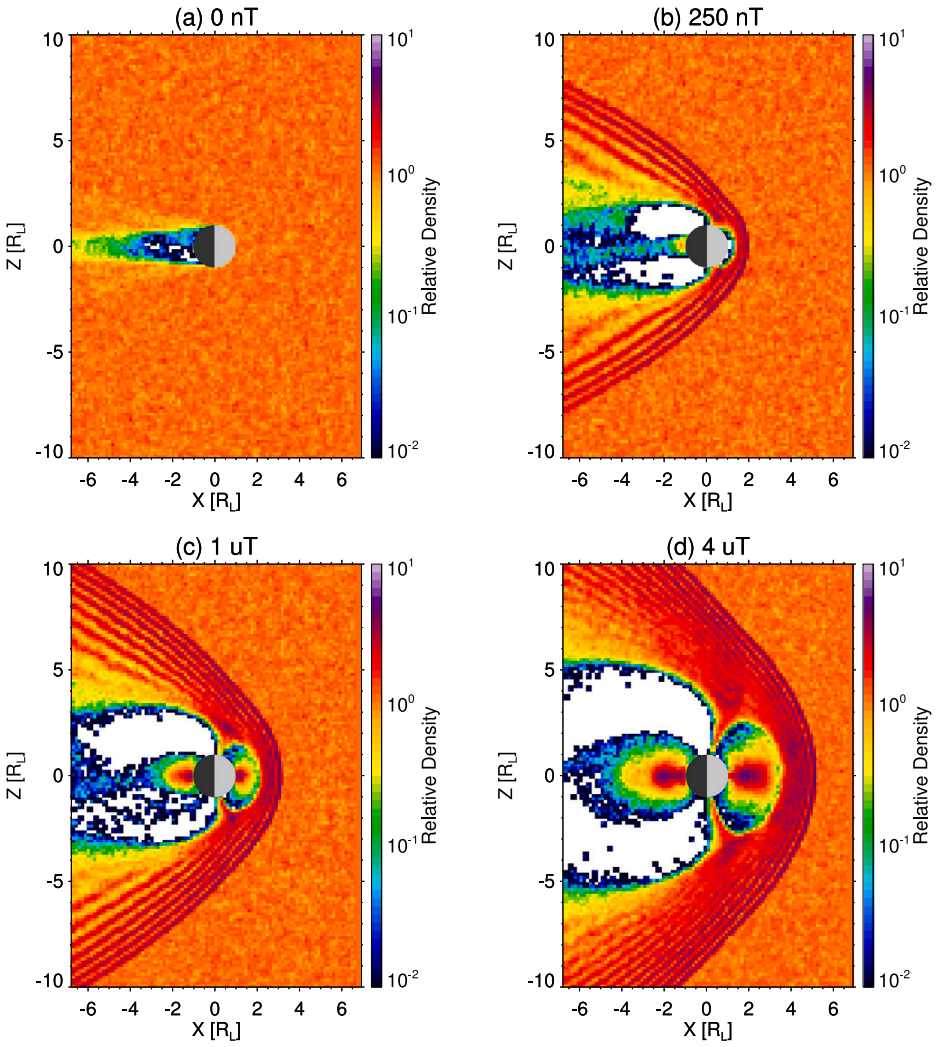

Fig. 2. Density distributions of solar wind $^{36}Ar^{+}$ in the x-z SSE plane for four paleomagnetic field strengths. Values are normalized to the upstream solar wind $^{36}Ar^{+}$ density. White regions contained no hybrid model particles.

time (blue curve), we see that the lunar $^{40}Ar^{+}$ flux is higher than the solar wind $^{36}Ar^{+}$ flux for much of the solar system lifetime, up to ~3.3 Ga. To first order, this would comport with the empirical relationship observed between the lunar antiquity indicator and sample age in various Apollo samples (e.g., Eugster et al., 2001); however, as discussed above, significant evidence supports the long-term variation of the solar wind ^{36}Ar flux. In comparison, using either of the Vidotto (2021) or Wood et al. (2005) scalings for the time evolution of the solar wind $^{36}Ar^{+}$ flux, the $^{40}Ar/^{36}Ar$ ratios are always lower than 1.5 and 0.5, respectively, as seen in panel 1(b). These maximum values for the antiquity indicator are at least an order-of-magnitude less than that observed in the oldest dated samples for which $^{40}Ar/^{36}Ar$ ratios have been reported (e.g., Reynolds et al., 1974). Thus, on one hand, adopting a constant $^{36}Ar^{+}$ flux yields a satisfactory agreement with observed antiquity indicator values in lunar samples; however, on the other hand, the assumption of a flat ^{36}Ar flux is in tension with solar and astrophysical observations. If we are to take the observations of solar wind flux variability at face value, then additional effects must also be at play in governing the behavior of the antiquity indicator.

3.2. Effects of a lunar paleomagnetic field on solar wind minor ion flux

In a previous study (Poppe et al., 2021), we used a three-dimensional plasma hybrid model (Fatemi et al., 2017) to explore the effects of varying paleomagnetic field strengths on the dynamics of heavy, highly charged solar wind minor ions (e.g., $^{4}He^{2+}$, $^{20}Ne^{8+}$, $^{36}Ar^{9+}$, etc.) at the Moon in the presence of a lunar paleomagnetic field. These model results demonstrated that the lunar paleomagnetosphere has a strong effect on the flux of solar wind ions to the lunar surface, where the globally averaged flux of solar wind minor ions to the lunar surface can be suppressed by over an order of magnitude. We use these results to further explore and quantify the role that the lunar paleomagnetosphere has on the flux of solar wind ^{36}Ar ions, in particular, to the lunar surface.

Fig. 2 shows the densities for solar wind $^{36}Ar^{+}$ ions relative to their upstream densities in the X-Z SSE plane containing both the paleomagnetic dipole moment ($+\hat{z}$) and the Moon-Sun vector ($+\hat{x}$) for four different paleomagnetic field strengths: (a) 0 nT, (b) 250 nT, (c) 1 μT, and (d) 4 μT. For the 0 nT case, panel 2(a), the $^{36}Ar^{+}$ flux remains undisturbed upstream of the Moon and fully impacts the lunar dayside. Correspondingly, a downstream wake forms due to the absorption of ions on the lunar dayside. This case is essentially representative of today's lunar environment, notwithstanding smaller perturbations due to remanent lunar crustal magnetization (e.g., Lue et al., 2011; Fatemi et al., 2014; Poppe et al., 2017). Shown in panel 2(b), the presence of a 250 nT paleomagnetic field significantly alters the solar wind $^{36}Ar^{+}$ interaction with the Moon. Even for this relatively weak paleomagnetic field (about the strength of Mercury's present-day field (e.g., Anderson et al., 2011; Anderson et al.)), the solar wind $^{36}Ar^{+}$ is prevented from directly accessing the lunar dayside surface except

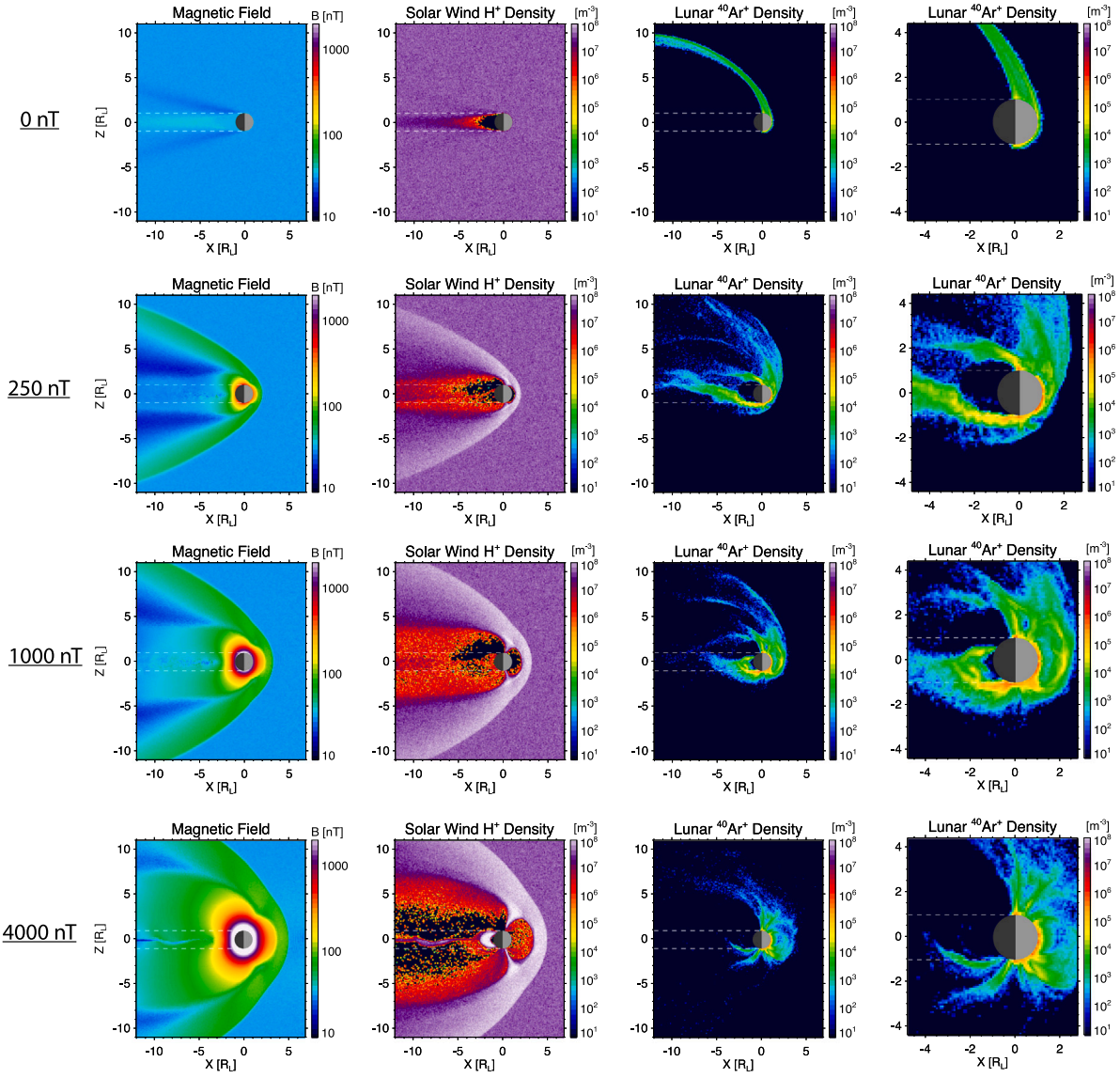

Fig. 3. The magnetic field magnitude, solar wind proton density, and lunar exospheric $^{40}Ar^{+}$ density (left, center, and right columns, respectively) in the X-Z SSE plane for 0, 250, 1000, and 4000 nT strength paleomagnetic fields. The right-most column displays a zoomed-in profile of the lunar exospheric $^{40}Ar^{+}$ density. The upstream IMF direction is into the page.

through high-latitude cusps. A small dayside magnetospheric cavity in the $^{36}Ar^{+}$ density develops as does a pair low-density lobes downstream of the Moon. Between the lobes on the lunar nightside, a thin current sheet forms allowing $^{36}Ar^{+}$ some access to the lunar nightside in the equatorial region.

As the paleomagnetic field strength is increased to 1 μT, shown in panel 2(c), the overall scale size of the magnetosphere increases. Similar to the 250 nT case, the solar wind $^{36}Ar^{+}$ is broadly prevented from accessing the lunar surface, except within the high-latitude cusps and the equatorial region. In contrast to the 250 nT case, however, the larger magnetospheric cavity allows for the formation of trapped (or at least *quasi*-trapped) particle belts in the equatorial, inner-magnetospheric regions (e.g., see also Oran et al., 2021). As discussed in Poppe et al. (2021), these trapped regions nevertheless allow for solar wind $^{36}Ar^{+}$ precipitation to the surface of the Moon due to their close proximity. Finally, in the 4 μT case, panel 2(d), the overall structure of the solar wind $^{36}Ar^{+}$ density is qualitatively similar to that for 1 μT but enlarged further. Solar wind $^{36}Ar^{+}$ ions are only able to precipitate to the lunar surface in the high-latitude cusps and via precipitation in the equatorial region while in trapped orbits, although we note that the trapped regions have moved farther from the surface resulting in less precipitation. In the particular case of solar wind $^{36}Ar^{+}$, paleomagnetic suppression factors ranged from ~20% for 62 nT-strength fields to ~90% for 4000 nT-strength fields (discussed further below in Section 5). These simulations thus indicate that the assumption of universal access of solar wind ions to the lunar surface is not tenable in the presence of lunar paleomagnetic fields (e.g., see also Tikoo et al., 2017; Poppe et al., 2021), notwithstanding any additional possible variations in the upstream solar wind flux as discussed above in Section 3.1.

4. Assessing the flux of ^{40} Ar^{+} to the lunar surface

Having explored the possible variations in the flux of solar wind $^{36}Ar^{+}$ to the lunar surface due to either long-term variations in the solar wind flux or the presence of a lunar paleomagnetosphere in Section 3 above, we now turn to an assessment of the flux of radiogenic $^{40}Ar^{+}$ to the lunar surface. As proposed in Manka and Michel (1970), the presence of trapped ^{40}Ar within lunar soil samples most likely originates from exospheric recycling after outgassing from the lunar

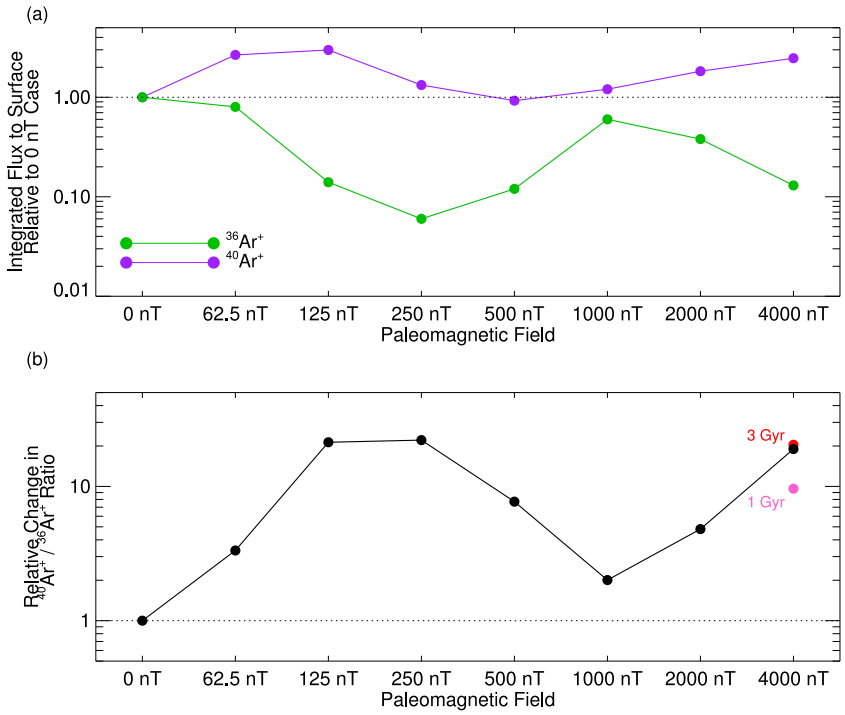

Fig. 4. (a) The flux of solar wind $^{36}Ar^+$ and lunar exospheric $^{40}Ar^+$ ions to the lunar surface as a function of the paleomagnetic field strength, relative to the flux in the unmagnetized (0 nT) case. (b) The $^{40}Ar^+/^{36}Ar^+$ flux ratio, again relative to the 0 nT case, demonstrating that paleomagnetic fields can bias the antiquity ratio up to a factor of ~20× high. In the 4000 nT case, the red and pink points denote the relative change in the $^{40}Ar^+/^{36}Ar^+$ flux ratio for solar wind conditions appropriate for 3 Gyr and 1 Gyr lunar ages, respectively.

interior. The underlying mechanism in this process is the presence of the solar wind convection electric field, $\mathbf{E_{sw}} = -\mathbf{v_{sw}} \times \mathbf{B_{imf}}$, where $\mathbf{v_{sw}}$ is the solar wind velocity and $\mathbf{B_{imf}}$ is the interplanetary magnetic field vector (although note that convection in the terrestrial magnetosphere has an analogous effect; e.g., Poppe et al., 2012; Cao et al., 2020; Liuzzo et al., 2021). Upon ionization, the lunar $^{40}Ar^+$ ions are accelerated by the convection electric field and those ions whose trajectories intersect the Moon are re-implanted into the lunar soil at typical energies in the keV range. Similar to the discussion of the flux of solar wind $^{36}Ar^+$ flux to the lunar surface above, the potential effects of a lunar paleomagnetosphere–which can significantly alter the near-surface electromagnetic environment of the Moon–on the recycling efficiency of lunar $^{40}Ar^+$ have not been fully quantified.

Model results for four different values of the paleomagnetic field strength (0 nT, 250 nT, 1000 nT, and 4000 nT) are shown in Fig. 3, including the magnetic field magnitude, solar wind proton density, and lunar $^{40}Ar^+$ density. As discussed in previous studies (e.g., Garrick-Bethell et al., 2019; Poppe et al., 2021) and seen in Fig. 2, the size of the lunar paleomagnetosphere increases as a function of the surface field strength, notable in both the magnetic field strength (left-most column) and solar wind proton density (second-to-left column). Of interest for this study is the distribution of lunar exospheric $^{40}Ar^+$ ions as a function of paleomagnetic field strength, seen in the two columns on the right (note that the right-most column displays a zoomed-in distribution for the $^{40}Ar^+$ ions). For the 0 nT case, the $^{40}Ar^+$ ion distribution appears as a classical cycloidal plume as the ions are picked up and accelerated into the bulk solar wind flow (see, e.g., Hartle and Killen, 2006; Poppe et al., 2022). A large fraction of those $^{40}Ar^+$ ions born on the -Z hemisphere of the Moon are reaccelerated into the Moon, as described by Manka and Michel (1970), while those ions on the +Z hemisphere escape the Moon entirely. Note that while the detailed distribution of these escaping ions varies as a function of solar wind and interplanetary magnetic field conditions, the first-order shape (i.e., a plume) remains constant.

In the 250 nT case, the distribution of $^{40}Ar^+$ ions is significantly disturbed by the presence of the lunar paleomagnetosphere. A small fraction of $^{40}Ar^+$ ions still undergo pickup and acceleration along a typical cycloidal trajectory similar to the 0 nT case. Such ions are those from the uppermost scale heights of the neutral ^{40}Ar distribution where the solar wind or magnetosheath convection is sufficient enough to fully pick the ions up. In contrast to the 0 nT case, $^{40}Ar^+$ ion outflow is observed immediately downstream of the Moon mainly in two large plumes for those ions born within the paleomagnetosphere itself. This behavior is generally similar to that seen in planetary Na^+ ion energization and transport at Mercury (e.g., Glass et al., 2021). Relatively higher densities of $^{40}Ar^+$ ions compared to the 0 nT are also seen very close to the lunar surface, likely due to less effective convection at low altitudes.

The $^{40}Ar^+$ ion distributions for the 1000 nT case share several features with the 250 nT case, including acceleration of a small fraction of $^{40}Ar^+$ ions along trajectories in the upstream solar wind and a series of plumes immediately downstream from the Moon. Densities near to the lunar surface are increased again over those seen in the 250 nT case, indicating enhanced trapping of $^{40}Ar^+$ ions within the inner paleomagnetosphere. Finally, in the 4000 nT case, little-to-no $^{40}Ar^+$ ions are seen picked up in the upstream solar wind although some escape is seen through the magnetosheath. $^{40}Ar^+$ ions are trapped at even higher densities near to the lunar surface while the strength and extent of plumes immediately downstream of the Moon are weaker than those in the 250 nT and 1000 nT cases. Overall, the behavior of $^{40}Ar^+$ ions in a 4000 nT paleomagnetic field is starkly different from the behavior of such ions in the absence of a paleomagnetic field. Thus, similar to our conclusions in Section 3.2 regarding solar wind $^{36}Ar^+$ ions, we find that the presence of a paleomagnetosphere must be accounted for in assessing the recycling flux of $^{40}Ar^+$ ions to the lunar surface as part of the antiquity indicator.

5. Analysis and discussion

The modeling results shown in Sections 3 and 4 demonstrate that the presence of a lunar paleomagnetosphere has strong effects on the flux of both solar wind $^{36}Ar^+$ ions and lunar exospheric $^{40}Ar^+$ ions to the lunar surface. To better quantify the net effect of the lunar paleomagnetosphere on the flux of both solar wind $^{36}Ar^+$ and lunar exospheric $^{40}Ar^+$ ions to the lunar surface, we have averaged the flux of both species over the entire lunar surface as a function of paleomagnetic field strength and normalized such fluxes to the respective flux for no paleomagnetosphere. We remind the reader that the upstream solar wind conditions were kept constant across all simulations, thereby allowing such a comparison. As seen in Fig. 4(a), the relative flux of solar wind $^{36}Ar^+$ to the lunar surface (green curve) first decreases as a function of paleomagnetic field strength from 0 nT to 250 nT to a minimum of 6%, increases back to ~70% for field strengths of 1000 nT, and finally drops to ~12% for the maximum field strength of 4000 nT. The initial decline of the relative solar wind $^{36}Ar^+$ flux through field strengths of 250 nT is driven by deflection of the incident solar wind away from the lunar surface via the paleomagnetosheath. The subsequent rise in relative solar wind $^{36}Ar^+$ flux through 1000 nT and eventual decay at higher field strengths is driven by the quasi-trapped solar wind particles. These trapped ions first provide a source of low-latitude precipitation (e.g., see Fig. 2(c)) thereby increasing the solar wind precipitation flux, yet at higher paleomagnetic field strengths, the altitude of these trapped belts increases, moving the particles away from the surface and again decreasing the precipitating flux.

In contrast, Fig. 4(a) also shows that the lunar exospheric $^{40}Ar^+$ flux (purple curve) first increases to a relative value of ~3 for 125 nT, drops back down to just below unity at 500 nT, before finally increasing again to a relative value of ~2.5 for 4000 nT, in rough anti-correlation with the observed $^{36}Ar^+$ fluxes. While the overall tendency to increase the lunar exospheric $^{40}Ar^+$ flux is due to the presence of, e.g., smaller $^{40}Ar^+$ ion gyroradii and an increased presence of closed field lines, the dip in relative $^{40}Ar^+$ ion fluxes is likely to due a temporary enhancement in bulk ion outflow through the paleomagnetotail lobes (e.g., see the $^{40}Ar^+$ ion distribution for 1000 nT in Fig. 3). At the 4000 nT field strength closest to that expected during the majority of the Moon's lifetime (Tikoo et al., 2017), the flux of solar wind $^{36}Ar^+$ to the lunar surface is suppressed by nearly an order-of-magnitude while the recycled flux of lunar exospheric $^{40}Ar^+$ to the lunar surface is enhanced by a factor of ~ 2.5×. Thus, as shown in Fig. 4(b), the presence of the lunar paleomagnetosphere–even in the absence of changes in the upstream solar wind flux–strongly biases the $^{40}Ar/^{36}Ar$ ratio. Such biases are most strongly present at field strengths of 125 to 250 nT, where the relative $^{40}Ar/^{36}Ar$ ratio is slightly greater than a factor of 20, and again at 4000 nT, where the relative $^{40}Ar/^{36}Ar$ ratio is just slightly less than 20.

The results shown in Fig. 4 provide a path for understanding how the $^{40}Ar/^{36}Ar$ antiquity indicator may operate in the presence of a lunar paleomagnetic field. Referring back to Fig. 1, adopting the time-variable behavior in the solar wind flux (e.g., Wood et al., 2005; Vidotto, 2021) rather than the assumption of constant flux would predict a much lower antiquity indicator (i.e., due to a higher $^{36}Ar^+$ flux to the Moon), inconsistent with observations (e.g., Reynolds et al., 1974; Eugster et al., 2001). In the presence of a paleomagnetic field, however, this increased flux of solar wind $^{36}Ar^+$ upstream of the Moon at earlier epochs is attenuated by the lunar paleomagnetic fields before striking the lunar surface. Additionally, an increased recirculation of lunar exospheric $^{40}Ar^+$ in the presence of the paleomagnetosphere can also mitigate the increased upstream solar-wind $^{36}Ar^+$ flux.

Indeed, this idea holds in a semi-quantitative sense by inspecting the relative changes in both the upstream solar wind $^{36}Ar^+$ flux and the efficiency of solar wind $^{36}Ar^+$ precipitation at an example solar system age of 2.5 Ga. As seen in Fig. 1, the Vidotto (2021) and Wood et al. (2005) models predict solar wind flux increases of ~4× and ~8× the present-day value, respectively. In contrast, the solar wind $^{36}Ar^+$ precipitation to the lunar surface at 2.5 Ga, governed by a paleomagnetic field strength of ~4000 nT (Tikoo et al., 2017), is reduced to a factor of ≈0.12 (≈1/8) that of the 0 nT case, as seen in Fig. 4(a). Increased recycling of lunar $^{40}Ar^+$ may also affect the antiquity indicator, but to a lesser extent that the paleomagnetic shielding of solar wind $^{36}Ar^+$. Nevertheless, within a first-order estimation, the increased solar wind $^{36}Ar^+$ flux is balanced by the decreasing solar wind $^{36}Ar^+$ precipitation efficiency, thereby allowing the antiquity indicator to more closely follow the natural radioactive decay profile of ^{40}K into ^{40}Ar.

We do note that this correlation may not hold as closely at other epochs in the Moon's lifetime, as one would not necessarily expect the lunar paleomagnetic field strength and solar wind flux to be exactly correlated with one another. Additionally, the primary set of simulations presented here have only used upstream solar wind conditions (i.e., density, speed, temperature) best estimated for a ~2 Gya epoch (Airapetian and Usmanov, 2016). Thus, we would need to explore the behavior of both $^{36}Ar^+$ and $^{40}Ar^+$ ions as a function of variability in the upstream solar wind conditions to fully characterize the behavior of the antiquity indicator at other epochs in lunar history. To assess this possible effect to first order, Fig. 4(b) shows the relative change in the $^{40}Ar/^{36}Ar$ ratio in the presence of a 4000 nT paleomagnetic field for solar wind conditions appropriate for 1 Gyr and 3 Gyr, respectively (see description of these conditions in Section 2), denoted by the pink and red dots. In the case of 3 Gyr conditions, the relative change in the $^{40}Ar/^{36}Ar$ ratio (20.4) is very close to that seen in the 2 Gyr conditions (19.0; i.e., the black point). In the case of the 1 Gyr conditions, the relative change in the $^{40}Ar/^{36}Ar$ ratio drops to 9.6. Closer inspection of the 1 Gyr results shows an increase in the amount of $^{40}Ar^+$ that can escape the lunar paleomagnetosphere. This effect is primarily due to the increased solar wind pressure that pushes the magnetospheric boundaries inward thereby exposing more $^{40}Ar^+$ to the magnetosheath and solar wind where they can be more efficiently picked up and lost to the solar wind, rather than being reimplanted in the lunar soil. One must also keep in mind that the lunar paleomagnetic fields likely ceased between ~1.92 and ~0.80 Gya (Mighani et al., 2020); thus, solar wind fluxes to the Moon during the latter-most portion of its lifetime should have no perturbations from the lunar paleomagnetosphere. Nevertheless, even approximately correlated decreases in both the paleomagnetic field and the solar wind flux over the lifetime of the solar system could still preserve the correlation seen in the lunar antiquity indicator in, e.g., Eugster et al. (2001), especially considering the relatively large error bars on most measured $^{40}Ar/^{36}Ar$ ratios.

Finally, we do also note that spatial variability in both the ^{36}Ar and ^{40}Ar precipitation fluxes to the lunar surface may introduction additional uncertainty in the ^{40}Ar /^{36}Ar ratio recorded in any given lunar sample. In the case of no paleomagnetic fields, both solar wind ^{36}Ar and lunar exospheric ^{40}Ar can precipitate nearly unimpeded on the dayside lunar surface and thus, to first order, can be considered homogeneous. In the presence of a paleomagnetosphere, however, the specific precipitation patterns are likely to be altered due to the interaction of both ^{36}Ar and ^{40}Ar ions with the paleomagnetic fields. Indeed, in a previous study, Poppe et al. (2021) presented results for the spatial precipitation patterns of a wide range of solar wind minor ions in the presence of a 1 μT paleomagnetic field (see their Figure 6). These results showed that solar wind minor ions, including $^{36}Ar^{n+}$, precipitated to the lunar surface both through the open magnetospheric cusps (e.g., similar to that observed at Mercury; Raines et al., 2022) and at lower equatorial latitudes due to particle trapping in the inner dipolar region of the paleomagnetosphere. Thus, it does appear possible that local variations in the precipitating ^{36}Ar and ^{40}Ar fluxes may be present during periods with a lunar paleomagnetosphere; however, the precipitation of ^{36}Ar ions in the equatorial region of the Moon and not just in the high-latitude cusps may mitigate this possible effect to a

large degree. Future work exploring the spatial variability of both the ^{36}Ar and ^{40}Ar fluxes to the lunar surface is clearly warranted.

6. Conclusion

The simulations presented here have shown that the presence of a lunar paleomagnetosphere drastically alters the flux of both solar wind $^{36}Ar^{+}$ and lunar exospheric $^{40}Ar^{+}$ ions to the lunar surface. With increasing paleomagnetic field strengths, solar wind $^{36}Ar^{+}$ ions are diverted away from the lunar surface via the magnetosheath, with surface precipitation generally only available through either the high-latitude magnetic cusps or low-latitude trapped particle belts. At paleomagnetic field strengths of 4 μT, which have been estimated to exist for a bulk of the Moon's lifetime (Tikoo et al., 2017), solar wind $^{36}Ar^{+}$ ion flux to the lunar surface is suppressed by nearly an order-of-magnitude. In contrast, the recycling efficiency of lunar exospheric $^{40}Ar^{+}$ ions back into the lunar surface is enhanced by the presence of a paleomagnetosphere, with a nearly three-fold increase seen in the case of 4 μT fields.

Our understanding of the lunar ^{40}Ar/^{36}Ar antiquity indicator is thus shaped by the results of these simulations. In the presence of a lunar paleomagnetosphere, assumptions on the constancy of both the solar wind flux to the lunar surface and the lunar exospheric recycling efficiency are not supported. Despite this, the observed near-correlation of the ^{40}Ar/^{36}Ar ratio with the radioactive decay profile of indigenous ^{40}K at the Moon (e.g., Eugster et al., 2001) is instead maintained by accounting for the likely secular decrease of the bulk solar wind flux over the Sun's lifetime (Wood et al., 2005; Vidotto, 2021). Indeed, the presence of greater solar wind fluxes at earlier epochs would in fact *require* a mechanism such as the lunar paleomagnetosphere for diminishing the precipitation of solar wind species to the lunar surface.

CRediT authorship contribution statement

A.R. Poppe: Conceptualization, Formal analysis, Funding acquisition, Investigation, Methodology, Resources, Writing – original draft. **I. Garrick-Bethell:** Conceptualization, Funding acquisition, Investigation, Project administration, Writing – review & editing. **S. Fatemi:** Conceptualization, Formal analysis, Investigation, Methodology, Resources, Software, Writing – review & editing. **C. Grava:** Investigation, Methodology, Writing – review & editing.

Declaration of competing interest

The authors declare that they have no known competing financial interests or personal relationships that could have appeared to influence the work reported in this paper.

Data availability

Data will be made available on request.

Acknowledgments

A.R.P. and I.G.-B. acknowledge support through NASA's Solar System Workings program, grant #80NSSC19K0560. A.R.P. thanks A. Vidotto for helpful conversations on the nature of the solar wind flux over time. S.F. acknowledges support from the Swedish National Space Agency (SNSA) grant 115/18 and the Swedish Research Council (VR) grant 2018-03454. The computations were enabled by the computational and storage resources on the Kebnekaise super-computer at the High Performance Computing Center North (HPC2N), Umeå University, Sweden. The authors thank two reviewers for constructive comments that improved the manuscript.

References

Airapetian, V.S., Usmanov, A.V., 2016. Reconstructing the solar wind from its early history to current epoch. Astrophys. J. Lett. 817, L24–L29.
Anderson, B.J., Johnson, C.L., Korth, H., Purucker, M.E., Winslow, R.M., Slavin, J.A., Solomon, S.C., McNutt, Jr., R.L., Raines, J.M., Zurbuchen, T.H., 2011. The global magnetic field of mercury from MESSENGER orbital observations. Science 333, 1859–1862.
Anderson, B.J., Johnson, C.L., Korth, H., Winslow, R.M., Borovsky, J.E., Purucker, M.E., Slavin, J.A., Solomon, S.C., Zuber, M.T., McNutt, Jr., R.L., Low-degree structure in mercury's planetary magnetic field. J. Geophys. Res. 117 (E00L12), 2012.
Ayres, T.R., 1997. Evolution of the solar ionizing flux. J. Geophys. Res. 103 (E1), 1641–1651. http://dx.doi.org/10.1029/96JE03306.
Becker, R.H., Pepin, R.O., 1989. Long-term changes in solar wind elemental and isotopic ratios: A comparison of two lunar ilmenites of different antiquities. Geochim. Cosmochim. Acta 53, 1135–1146.
Benna, M., Mahaffy, P.R., Halekas, J.S., Elphic, R.C., Delory, G.T., 2015. Variability of helium, neon, and argon in the lunar exosphere as observed by the LADEE NMS instrument. Geophys. Res. Lett. 42.
Bochsler, P., 1987. Solar wind ion composition. Phys. Scr. T18, 55–60.
Bochsler, P., 2000. Abundances and charge states of particles in the solar wind. Rev. Geophys. 38 (2), 247–266.
Bochsler, P., 2007. Minor ions in the solar wind. Astron. Astrophys. Rev. 14, 1–40. http://dx.doi.org/10.1007/s00159-006-0002-x.
Cao, X., Halekas, J., Poppe, A., Chu, F., Glassmeier, K.-H., 2020. The acceleration of lunar ions by magnetic forces in the terrestrial magnetotail lobes. J. Geophys. Res.: Space Phys. 125, http://dx.doi.org/10.1029/2020JA027829.
Cournède, C., Gattacceca, J., Rochette, P., 2012. Magnetic study of large apollo samples: Possible evidence for an ancient centered dipolar field on the moon. Earth Plan. Sci. Lett. 331–332, 31–42. http://dx.doi.org/10.1016/j.epsl.2012.03.004.
Curran, N.M., Joy, K.H., Snape, J.F., Pernet-Fisher, J.F., Gilmour, J.D., Nemchin, A.A., Whitehouse, M.J., Burgess, R., 2019. The early geological history of the moon inferred from ancient lunar meteorite miller range 13317. Meteorit. Planet. Sci. 54 (7), 1401–1430. http://dx.doi.org/10.1111/maps.13295.
Dmitriev, A.V., Suvorova, A.V., Veselovsky, I.S., 2011. Statistical characteristics of the heliospheric plasma and magnetic field at earth's orbit during four solar cycles 20-23. In: Johannson, H.E. (Ed.), Handbook on Solar Wind: Effects, Dynamics, and Interactions. NOVA Science Publishers, New York, NY, USA, pp. 81–144, chapter 2.
Dyal, P., Parkin, C.W., Daily, W.D., 1974. Magnetism and the interior of the moon. Rev. Geophys. Space Phys. 12 (4), 568–591.
Eugster, O., 2003. Cosmic-ray expsosure ages of meteorites and lunar rocks and their significance. Chem. Erde 63, 3–30. http://dx.doi.org/10.1078/0009-2819-00021.
Eugster, O., Beer, J., Burger, M., Finkel, R.C., Hofmann, H.J., Krähenbühl, U., Michel, T., Synal, H.A., Wölfli, W., 1991. History of the paired lunar meteorites MAC88104 and MAC88105 derived from noble gas isotopes, radionuclides, and some chemical abundances. Geochim. Cosmochim. Acta 55 (11), 3139–3148. http://dx.doi.org/10.1016/0016-7037(91)90478-N.
Eugster, O., Terribilini, D., Polnau, E., Kramers, J., 2001. The antiquity indicator argon-40/argon-36 for lunar surface samples calibrated by uranium-235–xenon136 dating. Meteorit. Planet. Sci. 36, 1097–1115.
Evans, A.J., Tikoo, S.M., 2022. An episodic high-intensity lunar core dynamo. Nature Astron. 6, 325–330. http://dx.doi.org/10.1038/s41550-021-01574-y.
Fatemi, S., Holmström, M., Futaana, Y., Lue, C., Collier, M.R., Barabash, S., Stenberg, G., 2014. Effects of protons reflected by lunar crustal magnetic fields on the global lunar plasma environment. J. Geophys. Res.: Space Phys. 119.
Fatemi, S., Poppe, A.R., 2018. Solar wind plasma interaction with asteroid 16 psyche: implication for formation theories. Geophys. Res. Lett. 45.
Fatemi, S., Poppe, A.R., Barabash, S., 2020. Hybrid simulations of solar wind proton precipitation to the surface of mercury. J. Geophys. Res.: Space Phys. 125, http://dx.doi.org/10.1029/2019JA027706.
Fatemi, S., Poppe, A.R., Delory, G.T., Farrell, W.M., 2017. AMITIS: A 3D GPU-based hybrid-PIC model for space and plasma physics. J. Phys.: Conf. Ser. 837.
Fatemi, S., Poppe, A.R., Vorburger, A., Lindkvist, J., Hamrin, M., 2022. Ion dynamics at the magnetopause of ganymede. J. Geophys. Res.: Space Phys. 127, http://dx.doi.org/10.1029/2021JA029863.
Fionnagáin, D.Ó., Vidotto, A.A., 2018. The solar wind in time: A chance in the behaviour of older winds. Mon. Not. R. Astron. Soc. 476, 2465–2475. http://dx.doi.org/10.1093/mnras/sty394.
Garrick-Bethell, I., Kelley, M.R., 2019. Reiner Gamma: A magnetized elliptical disk on the moon. Geophys. Res. Lett. 46, 5065–5074. http://dx.doi.org/10.1029/2019GL082427.
Garrick-Bethell, I., Poppe, A.R., Fatemi, S., 2019. The lunar paleo-magnetosphere: Implications for the accumulation of polar volatile deposits. Geophys. Res. Lett. 46, http://dx.doi.org/10.1029/2019GL082548.
Garrick-Bethell, I., Weiss, B.P., Shuster, D.L., Buz, J., 2009. Early lunar magnetism. Science 323, 356–359.
Garrick-Bethell, I., Weiss, B.P., Shuster, D.L., Tikoo, S.M., Tremblay, M.M., 2017. Further evidence for early lunar magnetism from troctolite 76535. J. Geophys. Res.: Planets 122, 76–93.

Geiss, J., Bochsler, P., 1991. Long-time variations in the solar wind properties: possible causes versus observations. In: Sonett, C.P., Giampapa, M.S., Matthews, M.S. (Eds.), The Sun in Time. In: Space Sciences Series, Univ. of Arizona Press, pp. 98–117.

Glass, A.N., Raines, J.M., Jia, X., Tenishev, V., Shou, Y., Aizawa, S., Slavin, J.A., 2021. A 3D MHD-particle tracing model of Na^+ energization on mercury's dayside. J. Geophys. Res.: Space Phys. 126, http://dx.doi.org/10.1029/2021JA029587.

Grava, C., Chaufray, J.-Y., Retherford, K.D., Gladstone, G.R., Greathouse, T.K., Hurley, D.M., Hodges, R.R., Bayless, A.J., Cook, J.C., Stern, S.A., 2015. Lunar exospheric argon modeling. Icarus 255, 135–147. http://dx.doi.org/10.1016/j.icarus.2014.09.029.

Güdel, M., 2007. The sun in time: Activity and environment. Living Rev. Sol. Phys. 4 (3), http://dx.doi.org/10.12942/lrsp-2007-3.

Hartle, R.E., Killen, R., 2006. Measuring pickup ions to characterize the surfaces and exospheres of planetary bodies: Applications to the moon. Geophys. Res. Lett. 33 (L05201).

Haviland, H., Poppe, A.R., Fatemi, S., Delory, G.T., de Pater, I., 2019. Time-dependent hybrid plasma simulations of lunar electromagnetic induction in the solar wind. Geophys. Res. Lett. 46, 4151–4160.

Heymann, D., Yaniv, A., Adams, J.A.S., Fryer, G.E., 1970. Inert gases in lunar samples. Science 167, 555–558. http://dx.doi.org/10.1126/science.167.3918.555.

Hodges, R.R., Hoffman, J.H., Johnson, F.S., 1974. The lunar atmosphere. Icarus 21, 415–426.

Hodges, R.R., Hoffman, J.H., Johnson, F.S., Evans, D.E., 1973. Composition and dynamics of lunar atmosphere. In: Proc. 4th Lunar Sci. Conf., vol. 3, pp. 2855–2864.

Hodges, R.R., Mahaffy, P.R., 2016. Synodic and semiannual oscillations of argon-40 in the lunar exosphere. Geophys. Res. Lett. 43.

Hood, L.L., Zakharian, A., Halekas, J., Mitchell, D.L., Lin, R.P., Acuña, M.H., Binder, A.B., 2001. Initial mapping and interpretation of lunar crustal magnetic anomalies using lunar prospector magnetometer data. J. Geophys. Res. 106 (11), 27 825–27, 839.

Jardine, M., Collier Cameron, A., 2019. Slingshot prominences: nature's wind gauges. Mon. Not. R. Astron. Soc. 482, 2853–2860. http://dx.doi.org/10.1093/mnras/sty2872.

Joy, K.H., Kring, D.A., Bogard, D.D., McKay, D.S., Zolensky, M.E., 2011. Re-examination of the formation ages of the apollo 16 regolith breccias. Geochim. Cosmochim. Acta 75, 7208–7225. http://dx.doi.org/10.1016/j.gca.2011.09.018.

Joy, K.H., Zolensky, M.E., Nagashima, K., Huss, G.R., Ross, D.K., McKay, D.S., Kring, D.A., 2012. Direct detection of projectile relics from the end of the lunar basin-forming epoch. Science 336, http://dx.doi.org/10.1126/science.1219633.

Kegerreis, J.A., Eke, V.R., Massey, R.J., Beaumont, S.K., Elphic, R.C., Teodoro, L.F., 2017. Evidence for a localised source of the argon in the lunar exosphere. J. Geophys. Res.: Planets 122, 2163–2181.

Killen, R.M., 2002. Source and maintenance of the argon atmospheres of mercury and the moon. Meteorit. Planet. Sci. 37, 1223–1231.

Kirsten, T., Horn, P., Kiko, J., 1973.^{39}Ar–^{40}Ar dating and rare gas analysis of apollo 16 rocks and soils. In: Proc. 4th Lunar Sci. Conf., vol. 2, pp. 1757–1784.

Ledvina, S.A., Ma, Y.-J., Kallio, E., 2008. Modeling and simulating flowing plasmas and related phenomena. Space Sci. Rev. 139, 143–189. http://dx.doi.org/10.1007/s11214-008-9384-6.

Liuzzo, L., Poppe, A.R., Halekas, J.S., Simon, S., Cao, X., 2021. Investigating the moon's interactions with the terrestrial magnetotail lobe plasma. Geophys. Res. Lett. 48, http://dx.doi.org/10.1029/2021GL093566.

Lucey, P., Korotev, R.L., Gillis, J.J., Taylor, L.A., Lawrence, D., Campbell, B.A., Elphic, R., Feldman, W.C., Hood, L.L., Hunten, D.M., Mendillo, M., Noble, S., Papike, J.J., Reedy, R.C., Lawson, S., Prettyman, T., Gasnault, O., Maurice, S., 2006. Understanding the lunar surface and space-moon interactions. Rev. Min. Geochem. 60, 83–219.

Lue, C., Futaana, Y., Barabash, S., Wieser, M., Holmström, M., Bhardwaj, A., Dhanya, M.B., Wurz, P., 2011. Strong influence of lunar crustal fields on the solar wind flow. Geophys. Res. Lett. 38 (L03202).

Manka, R.H., Michel, F.C., 1970. Lunar atmosphere as a source of argon-40 and other lunar surface elements. Science 169 (3942), 278–280.

McKay, D.S., Bogard, D.D., Morris, R.V., Korotev, R.L., Johnson, P., Wentworth, S.J., 1986. Apollo 16 regolith breccias: Characterization and evidence for early formation in the mega-regolith. J. Geophys. Res. 91 (B4), D277–D303.

Merle, R.E., Nemchin, A.A., Whitehouse, M.J., Pidgeon, R.T., Grange, M.L., Snape, J.F., Thiessen, F., 2017. Origin and transportation history of lunar breccia 14311. Meteorit. Planet. Sci. 52 (5), 842–858. http://dx.doi.org/10.1111/maps.12835.

Mighani, S., Wang, H., Shuster, D.L., Borlina, C.S., Nichols, C.I.O., Weiss, B.P., 2020. The end of the lunar dynamo. Sci. Adv. 6, http://dx.doi.org/10.1126/sciadv.aax0883.

Mitchell, D.L., Halekas, J.S., Lin, R.P., Frey, S., Hood, L.L., Acuña, M.H., Binder, A., 2008. Global mapping of lunar crustal magnetic fields by lunar prospector. Icarus 194, 401–409.

Obase, T., Nakashima, D., 2023. Past solar wind flux recorded in solar-gas-rich meteorites. Icarus 389, http://dx.doi.org/10.1016/j.icarus.2022.115290.

Oran, R., Weiss, B.P., de Soria Santacruz-Pich, M., Jun, I., Lawrence, D.J., Polanskey, C.A., Ratliff, J.M., Raymond, C.A., Ream, J.B., Russell, C.T., Shprits, Y.Y., Zuber, M.T., Elkins-Tanton, L.T., 2021. Maximum energies of trapped particles around magnetized planets and small bodies. Geophys. Res. Lett. 49, http://dx.doi.org/10.1029/2021GL097014.

Podosek, F.A., Huneke, J.C., 1973. Argon in apollo 15 green glass spherules (15426):^{40}Ar– ^{39}Ar age and trapped argon. Earth Plan. Sci. Lett. 19, 413–421.

Poppe, A.R., Fatemi, S., 2023. The solar wind interaction with (1) ceres: The role of interior conductivity. Plan. Sci. J. 4.

Poppe, A.R., Garrick-Bethell, I., Fatemi, S., 2021. Fractionation of solar wind minor ion precipitation by the lunar paleomagnetosphere. Plan. Sci. J. 2 (60), http://dx.doi.org/10.3847/PSJ/abea7d.

Poppe, A.R., Halekas, J.S., Harada, Y., 2022. A comprehensive model for pickup ion formation at the moon. J. Geophys. Res.: Planets 127, http://dx.doi.org/10.1029/2022JE007422.

Poppe, A.R., Halekas, J.S., Lue, C., Fatemi, S., 2017. ARTEMIS observations of the solar wind proton scattering function from lunar crustal magnetic anomalies. J. Geophys. Res.: Planets 122.

Poppe, A.R., Halekas, J.S., Sarantos, M., Delory, G.T., 2013. The self-sputtered contribution to the lunar exosphere. J. Geophys. Res. 118.

Poppe, A.R., Samad, R., Halekas, J.S., Sarantos, M., Delory, G.T., Farrell, W.M., Angelopoulos, V., McFadden, J.P., 2012. ARTEMIS observations of lunar pick-up ions in the terrestrial magnetotail. Geophys. Res. Lett. 39 (L17104).

Raines, J.M., Dewey, R.M., Staudacher, N.M., Tracy, P.J., Bert, C.M., Sarantos, M., Gershman, D.J., Jasinski, J.M., Bowers, C.F., Fisher, E., Slavin, J.A., 2022. Proton precipitation in mercury's northern magnetospheric cusp. J. Geophys. Res.: Space Phys. 127, http://dx.doi.org/10.1029/2022JA030397.

Rasca, A.P., Fatemi, S., Farrell, W.M., Poppe, A.R., Zheng, Y., 2021. A double disturbed lunar plasma wake. J. Geophys. Res.: Space Phys. 126, http://dx.doi.org/10.1029/2020JA028789.

Reisenfeld, D.B., Burnett, D.S., Becker, R.H., Grimberg, A.G., Heber, V.S., Hohenberg, C.M., Jurewicz, A.J.G., Meshik, A., Pepin, R.O., Raines, J.M., Schlutter, D.J., Wieler, R., Wiens, R.C., Zurbuchen, T.H., 2007. Elemental abundances of the bulk solar wind: Analyses from genesis and ACE. Space Sci. Rev. 130, 79–86.

Reisenfeld, D.B., Wiens, R.C., Barraclough, B.L., Steinberg, J.T., Neugebauer, M., Raines, J., Zurbuchen, T.H., 2013. Solar wind conditions and composition during the genesis mission as measured by in situ spacecraft. Space Sci. Rev. 175, 125–164.

Reynolds, J.H., Alexander, Jr., E.C., Davis, P.K., Srinivasan, B., 1974. Studies of K–Ar dating and xenon from extinct radioactivities in breccia 14318; implications for early lunar history. Geochim. Cosmochim. Acta 38 (3), 401–417. http://dx.doi.org/10.1016/0016-7037(74)90134-3.

Shea, E.K., Weiss, B.P., Cassata, W.S., Shuster, D.L., Tikoo, S.M., Gattacceca, J., Grove, T.L., Fuller, M.D., 2012. A long-lived lunar core dynamo. Science 335, 453–456.

Tikoo, S.M., Weiss, B.P., Shuster, D.L., Suavet, C., Wang, H., Grove, T.L., 2017. A two-billion-year history for the lunar dynamo. Sci. Adv. 3.

Vidotto, A.A., 2021. The evolution of the solar wind. Living Rev. Sol. Phys. 18 (3), http://dx.doi.org/10.1007/s41116-021-00029-w.

von Steiger, R., Schwadron, N.A., Fisk, L.A., Geiss, J., Gloeckler, G., Hefti, S., Wilken, B., Wimmer-Schweingruber, R.F., Zurbuchen, T.H., 2000. Composition of quasi-stationary solar wind flows from ulysses/solar wind ion composition spectrometer. J. Geophys. Res. 105 (A12), 27217–27238.

Wakita, S., Johnson, B.C., Garrick-Bethell, I., Kelley, M.R., Maxwell, R.E., Davidson, T.M., 2021. Impactor material records the ancient lunar magnetic field in antipodal anomalies. Nature Commun. 12, http://dx.doi.org/10.1038/s41467-021-26860-1.

Wang, X.-D., Fatemi, S., Nilsson, H., Futaana, Y., Holmström, M., Barabash, S., 2023. Solar wind interaction with mars: electric field morphology and source terms. Mon. Not. R. Astron. Soc. 521 (3), 3597–3607. http://dx.doi.org/10.1093/mnras/stad247.

Weiss, B.P., Tikoo, S.M., The lunar dynamo. Science 346 (6214), 2014.

Wieler, R., 1998. The solar noble gas record in lunar samples and meteorites. Space Sci. Rev. 85, 303–314.

Wieler, R., 2016. Do lunar and meteoritic archives record temporal variations in the composition of solar wind noble gases and nitrogen? A reassessment in the light of genesis data. Chem. Erde 76, 463–480. http://dx.doi.org/10.1016/j.chemer.2016.06.001.

Wieler, R., Heber, V.S., 2003. Noble gas isotopes on the moon. Space Sci. Rev. 106, 197–210.

Wieler, R., Humbert, F., Marty, B., 1999. Evidence for a predominantly non-solar origin of nitrogen in the lunar regolith revealed by single grain analyses. Earth Plan. Sci. Lett. 167, 47–60.

Wood, B.E., 2004. Astropheres and solar-like stellar winds. Living Rev. Sol. Phys. 1 (2), http://dx.doi.org/10.12942/lrsp-2004-2.

Wood, B.E., Müller, H.-R., Zank, G.P., Linksy, J.L., 2002. Measured mass-loss rates of solar-like stars as a function of age and activity. Astrophys. J. 574, 412–425Vi.

Wood, B.E., Müller, H.-R., Zank, G.P., Linksy, J.L., Redfield, S., 2005. New mass-loss measurements from astrospheric Lyα absorption. Astrophys. J. 628, L143–L146.

Yaniv, A., Heymann, D., 1972. Atmospheric Ar^{40} in lunar fines. In: Proc. 3rd Lunar Sci. Conf., vol. 2, pp. 1967–1980.